REVERSE TIME MIGRATION USING PHASE CROSS-CORRELATION

J. C. Costa, W. E. Medeiros, M. Schimmel, F. L. Santana, and J. Schleicher

email: *js@ime.unicamp.br*

keywords: *RTM, imaging condition, phase cross-correlation*

ABSTRACT

Improving the quality of Reverse Time Migration (RTM) images can be beneficial for seismic interpretation. We present and evaluate new imaging conditions for RTM, which are based on the phase coherence between the forward and backward propagated wavefields. These imaging conditions can be calculated simultaneously to conventional conditions at little or no extra cost. They make use of the instantaneous phase and envelope of the analytical signals of the source and receiver wavefields, besides the real wavefields. The availability of these fields at each image point enables several alternatives to define imaging conditions. We explore, in addition to pure phase cross-correlation, two approaches of amplitude-weighted phase cross-correlation. Our numerical experiments, imaging both synthetic and field data sets, show that these new imaging conditions can highlight weak reflectors by locally improving the resolution of RTM images, particularly in the deep portions of the seismic images. In addition, reflection events produced at discontinuities might be enhanced as sharp signals, suggesting that the proposed imaging conditions can help to delineate both stratigraphic and structural features that are harder to see in conventional images. These properties of the phase cross-correlation imaging conditions make them an interesting tool to provide additional information that can aid seismic interpretation in complex structural settings.

INTRODUCTION

Reverse Time Migration (RTM) has become the method of choice for seismic imaging in complex geological settings (Zhang and Sun, 2009). The capability of imaging without dip limitations and the absence of shadow zones have pushed its development. In addition, with a proper change in the boundary conditions for the forward propagated wavefield, it is possible even to obtain true amplitude angle-domain common image gathers (Zhang and Sun, 2009; Yan and Dickens, 2016). RTM images are currently viewed as the most faithful pictures of the earth's subsurface, and there is an increasing demand from interpreters for images showing more stratigraphic details (Etgen et al., 2009). Recent advances in RTM technology have focused on improving efficiency and image quality. The reduction of backscattering noise in RTM has been achieved with post-imaging filtering or through modified imaging conditions (Shen and Albertin, 2015; Wang et al., 2016; Moradpouri et al., 2017; Du et al., 2017). Other new imaging conditions can produce amplitude compensations or obliquity corrections, separate events based on their local space-time slope, and reduce backscattered noises (e.g. Guitton et al., 2007; Zhang et al., 2007; Sava, 2007; Schleicher et al., 2008; Chattopadhyay and McMechan, 2008; Costa et al., 2009).

While amplitude-correct images have gained importance in interpretation, sometimes additional, purely stratigraphic images with no amplitude information can be helpful for interpretation. They can allow to follow reflections, particularly in the deep portions of the seismic images, where amplitude information may become unreliable. In this work, we propose several variations of a new, purely phase-based imaging condition which aims at enhancing stratigraphic and structural features in RTM seismic images. The new imaging conditions require the propagation of the analytical signal of the source and receiver wavefields

instead of the usual real wavefields. As a consequence, we have, at each image point, both the amplitude and phase fields of the source and receiver wavefields, allowing the use of phase cross-correlation (PC) (Schimmel, 1999) to complement the classical cross-correlation (CC) through new mixed imaging conditions. It is important to note that the availability of the analytical wavefields can be used to decompose them into upward and downward-propagating components (Shen and Albertin, 2015; Wang et al., 2016). In this case, the PC-based imaging conditions can be calculated in addition to conventional imaging conditions at almost no additional cost.

PC measures the coherence of instantaneous phases (e.g. Bracewell, 1965) and it is explicitly amplitude unbiased. It is determined by the number of phase-coherent time samples. Therefore it has the potential to enhance weak locally coherent events which would hardly be resolved by CC; this is the motivation to use PC in an RTM imaging condition. Our numerical experiments, imaging both synthetic and field data sets, show that the new imaging conditions employing PC indeed improve the resolution of weak-amplitude events in RTM images. In addition, reflection events produced at discontinuities are enhanced as sharp signals, suggesting that the proposed imaging conditions help to better delineate both stratigraphic and structural features.

METHODOLOGY

Phase cross-correlation

PC is based on analytic-signal theory. Therein a complex trace $S(t) = s(t) + iH[s(t)]$ is constructed from the real time-series $s(t)$ and its Hilbert Transform

$$H[s(t)] = \frac{1}{\pi} \int_{-\infty}^{\infty} \frac{s(\tau)}{\tau - t} d\tau \,. \tag{1}$$

The Hilbert Transform functions as $\pi/2$-phase rotator to compute the orthonormal time-series of $s(t)$. The analytic signal is a unique time-dependent representation of the real-valued recorded seismic trace $s(t)$ in the complex domain. It is often expressed by means of an envelope function $A_S(t)$ and an instantaneous phase $\varphi_S(t)$, i.e., $S(t) = A_S(t) \exp[i\varphi_S(t)]$. The instantaneous phase characterizes the waveform complexities as a function of time and has been used to design the phase stack (Schimmel and Paulssen, 1997), an amplitude-unbiased phase-coherent measure based on the sum of phasors $\exp[i\varphi_S(t)]$.

Let $S(t)$ and $R(t)$ be two analytical signals associated with two time-series $s(t)$ and $r(t)$, respectively, with envelopes $A_S(t)$ and $A_R(t)$ and instantaneous phases $\varphi_S(t)$ and $\varphi_R(t)$. In analogy to CC, PC between $S(t)$ and $R(t)$ at time-lag τ in a time window $[t_0, t_0 + W]$ is defined as

$$PC(\tau, W; S, R; \nu) = \frac{1}{W} \int_{t_0}^{t_0+W} \Psi_\tau(\varphi_S(t), \varphi_R(t); \nu) \, dt, \tag{2}$$

where the expression

$$\Psi_\tau(\varphi_S(t), \varphi_R(t); \nu) = \frac{1}{2^\nu} \big[|\exp\{i\varphi_S(t+\tau)\} + \exp\{i\varphi_R(t)\}|^\nu$$
$$- |\exp\{i\varphi_S(t+\tau)\} - \exp\{i\varphi_R(t)\}|^\nu \big] \tag{3}$$

substitutes the product $\Phi_\tau(t) = s(t+\tau)r(t)$ appearing in classical CC. Above, W is the correlation window length and ν is a heuristic parameter which permits to tune the sensitivity of the phase stacks. Note that when two time series present high waveform similarity with the same polarity around lag τ, their phasors are approximately equal, $\varphi_R(t) \approx \varphi_S(t+\tau)$, so that expression 3 reduces to

$$\Psi_\tau(\varphi_S(t), \varphi_R(t); \nu) \approx \frac{1}{2^\nu} \big[|2\exp\{i\varphi_R(t)\}|^\nu - 0 \big] = 1 \,, \tag{4}$$

while for reverse polarity $\varphi_R(t) \approx -\varphi_S(t+\tau)$, resulting in

$$\Psi_\tau(\varphi_S(t), \varphi_R(t); \nu) \approx \frac{1}{2^\nu} \big[0 - |2\exp\{i\varphi_R(t)\}|^\nu \big] = -1 \,. \tag{5}$$

On the other hand, for two time series do not presenting waveform similarity around lag τ, PC (equation 2) represents a sum over sine and cosine functions, the integral over which approximates zero if the window is sufficiently large. In summary, PC is a real-valued functional which measures anti-correlated and correlated waveform similarity between -1 and 1, in full analogy to a normalized version of CC. For further details, please refer to Schimmel and Paulssen (1997) or Schimmel (1999).

PC has been successfully applied in seismic interferometry studies, where it improves the extraction of small signals (Schimmel et al., 2010) for monitoring or imaging. The monitoring studies benefit from the amplitude-unbiased approach through a fast convergence to a stable medium response and consequently improved time resolution (e.g., D'Hour et al., 2015). In seismic imaging studies, PC has been employed mainly for signal extraction, such as coda phases, to map upper mantle discontinuities (Bonatto et al., 2015) and empirical Green Functions for global ambient noise tomography (Haned et al., 2015). Gaudot et al. (2015) take advantage of PC's statistical properties to detect and image a noise source. To our knowledge, PC has not been used before to build RTM image conditions.

According to Schimmel (1999), PC shows higher sensitivity to coherence than classical CC, regardless of the event amplitude. This observation is in good qualitative agreement with the known fact that instantaneous phase, when used as a seismic attribute, shows finer layering details and improved reflection continuity (Barnes, 2007).

Phase cross-correlation imaging conditions

Let $p_S(\mathbf{x}, t)$ and $p_R(\mathbf{x}, t)$ denote the forward propagated source wavefield and the backward propagated receivers wavefield, respectively. Then, any imaging condition in RTM relies on the assumption that, for each shot, events in $p_S(\mathbf{x}, t)$ and $p_R(\mathbf{x}, t)$ should coincide in space and time at every scattering point in the subsurface (Claerbout, 1971). Given a migration velocity field consistent with the data, this condition can focus reflections and diffracted events at their correct position. The classical implementation of this assumption is a cross-correlation, i.e.,

$$I(\mathbf{x}) = \sum_S \int_0^T p_S(\mathbf{x}, t) p_R(\mathbf{x}, t) dt , \qquad (6)$$

where $I(\mathbf{x})$ represents the seismic image at a subsurface point $\mathbf{x}$, calculated using Claerbout's classical RTM imaging condition, and where T is the maximum recorded time. This original imaging condition has been revised by several authors aiming to improve the quality of RTM images (Yoon and Marfurt, 2006; Guitton et al., 2007; Zhang et al., 2007; Schleicher et al., 2008; Costa et al., 2009). Their contributions provide amplitude correction, reduction of the backscattered noise, better illumination compensation, and obliquity factor corrections.

If an additional image with improved reflector visibility is desirable, PC can be used to focus RTM images. In that case, it is necessary to propagate the analytical signals $P_S(\mathbf{x}, t)$ and $P_R(\mathbf{x}, t)$ associated with the source wavefield, $p_S(\mathbf{x}, t)$, and the receiver wavefield, $p_R(\mathbf{x}, t)$, into the subsurface. Then, at every time frame t and at every position $\mathbf{x}$ in the subsurface, the complex fields

$$P_R(\mathbf{x}, t) = A_R(\mathbf{x}, t) \exp\left[i\varphi_R(\mathbf{x}, t)\right] \qquad (7)$$

and

$$P_S(\mathbf{x}, t) = A_S(\mathbf{x}, t) \exp\left[i\varphi_S(\mathbf{x}, t)\right] \qquad (8)$$

are available.

With this information, the simplest PC-based imaging condition is to stack over the zero-lag version of PC in equation 2, i.e.,

$$
\begin{aligned}
I_{PC}(\mathbf{x}) &= \frac{1}{N_S} \sum_S PC(\tau = 0, T; P_R(\mathbf{x}, t), P_S(\mathbf{x}, t); \nu) \\
&= \frac{1}{N_S T} \sum_S \int_0^T \Psi_0(\varphi_S(\mathbf{x}, t), \varphi_R(\mathbf{x}, t); \nu) \, dt ,
\end{aligned}
\qquad (9)
$$

where N_S denotes the number of shots.

Several alternative imaging conditions can be conceived of, which make use of the two real wavefields $p_S(\mathbf{x}, t)$ and $p_R(\mathbf{x}, t)$ and the four analytical fields $A_R(\mathbf{x}, t)$, $\varphi_R(\mathbf{x}, t)$, $A_S(\mathbf{x}, t)$, and $\varphi_S(\mathbf{x}, t)$. In addition to the simple PC imaging condition of equation 9, we investigate the following variations: amplitude-weighted PC imaging condition

$$I_{PC}^p(\mathbf{x}) = \frac{\sum_S \int_0^T |p_S(\mathbf{x}, t) p_R(\mathbf{x}, t)| \Psi_0(\varphi_S(\mathbf{x}, t), \varphi_R(\mathbf{x}, t); \nu) dt}{\sum_S \int_0^T |p_S(\mathbf{x}, t) p_R(\mathbf{x}, t)| dt} \tag{10}$$

and envelope-weighted PC imaging condition

$$I_{PC}^A(\mathbf{x}) = \frac{\sum_S \int_0^T A_S(\mathbf{x}, t) A_R(\mathbf{x}, t) \Psi_0(\varphi_S(\mathbf{x}, t), \varphi_R(\mathbf{x}, t); \nu) dt}{\sum_S \int_0^T A_S(\mathbf{x}, t) A_R(\mathbf{x}, t) dt} \ . \tag{11}$$

Because imaging condition $I_{PC}(\mathbf{x})$ of equation 9 is based solely on pure PC, it does not depend on the wavefield amplitudes. In contrast, the amplitude and evelope-weighted PC imaging conditions $I_{PC}^p(\mathbf{x})$ and $I_{PC}^A(\mathbf{x})$ are both weighted averages of the zero-lag PC integrand $\Psi_0(\varphi_R, \varphi_S; \nu)$, which make use of amplitude information. For $I_{PC}^p(\mathbf{x})$, the weights are composed of the moduli of the real wavefields while for $I_{PC}^A(\mathbf{x})$ the weights are determined by the analytical envelope amplitudes. It must be stressed that the weights do not carry any phase information, but are simply designed to attenuate low-amplitude migration artifacts.

NUMERICAL EXPERIMENTS

Marmousi data

In order to investigate the properties of these new imaging conditions on RTM images, besides the effect of parameter ν, we performed numerical experiments using the Marmousi data set. As a reference for comparison, we use the CC images obtained with equation 6 and its illumination-compensated version, given by

$$I_{CC}(\mathbf{x}) = \frac{\sum_S \int_0^T p_S(\mathbf{x}, t) p_R(\mathbf{x}, t) dt}{< \sum_S \int_0^T p_S(\mathbf{x}, t) p_S(\mathbf{x}, t) dt >} \ , \tag{12}$$

where $< \cdot >$ represents a local averaging operation in a small window around position $\mathbf{x}$.

For our numerical tests in the 2D acoustic approximation, we computed the analytical solution of the acoustic wave equation using a finite-difference scheme of second order time and 14th order in space. In order to reduce numerical dispersion and numerical anisotropy we optimized the spatial operators according to Holberg (1987). The efficiency of the analytical-wavefield propagation can be further improved using the prescriptions of Pestana and Revelo (2017).

The migration velocity model (Figure 1b) is a smoothed version of the Marmousi velocity model (Figure 1a) sampled in a uniform grid with 12 m interval. The RTM images were computed with a Ricker source wavelet with peak frequency equal to 12 Hz. The averaging operation in equation 12 has been computed using a 5×5 square box around each imaging point.

Figure 2 shows the CC reference images with and 395 without illumination compensation (conditions 396 $I(\mathbf{x})$ in equation 397 6, and 398 $I_{CC}(\mathbf{x})$ in equation 12) and 399 Figure 3 shows the image produced using the PC 400 imaging condition (condition 401 $I_{PC}(\mathbf{x})$ in equation 9) with $\nu = 100$. In spite of the somewhat unstable first impression of the latter image, closer inspection reveals some interesting features, particularly in the deeper part of the image. For example, the geometry of the anticlines below 2 km depth is more easily recognizable. Also, some stratigraphic features are enhanced like, for instance, the layers around depth 1.5 km at position 4 km and around depth 2 km at position 7 km.

The rather unstable aspect of the image in Figure 3 is caused by the fact that the PC-based imaging condition of equation 9 is completely amplitude independent. As a result of this amplitude insensitivity, migration artifacts with low amplitudes in the reference images of Figure 2 are amplified. Overall, we conclude that although enhancing these kind of undesirable effects, a PC-based imaging condition can be useful to highlight structures that might be missed in a conventional image.

Distance (km)

(a)

Distance (km)

(b)
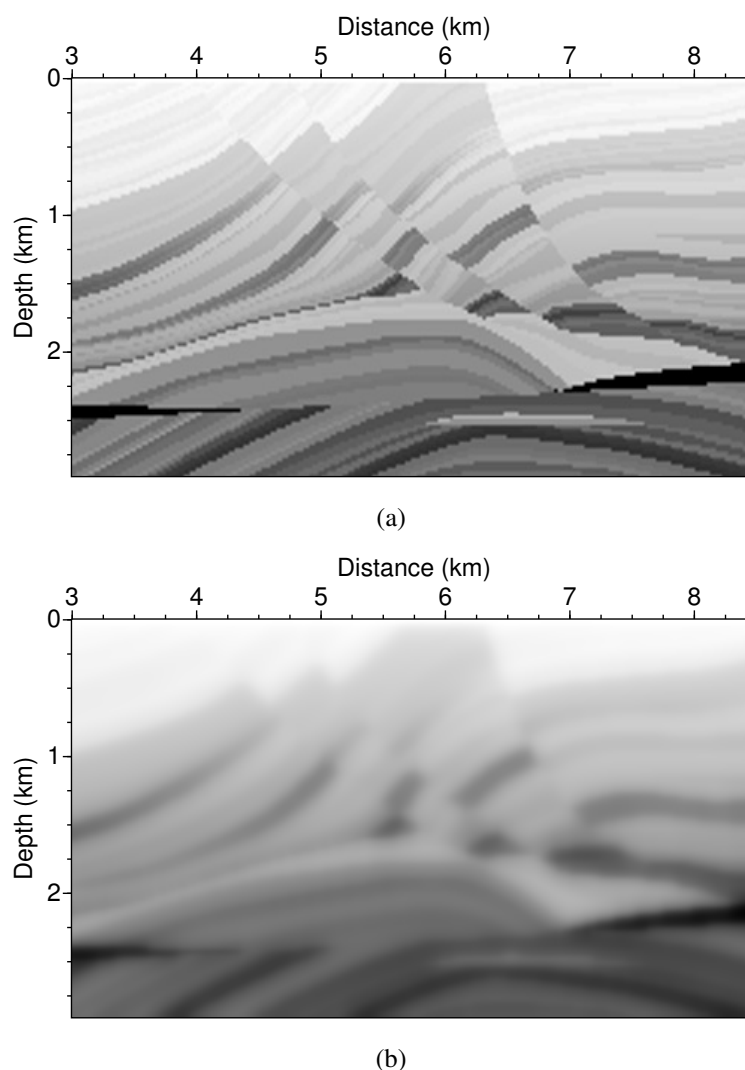
Figure 1: Marmousi velocity model. (a) True model. (b) Smoothed migration velocity model.

In order to take advantage of the high sensitive of the PC imaging condition while improving the robustness regarding artifacts, we studied the amplitude and envelope-weighted PC imaging conditions given by equations 10 and 11. The resulting images using $\nu = 100$ are shown in Figure 4. These images are indeed better interpretable, because most of the undesirable artifacts present in Figure 3 are strongly attenuated. The better stratigraphic quality, however, is preserved.

When compared with Figure 2, we may even say that the weighted-PC RTM images present some higher resolution features. As an example, the existence of the steeply dipping layers, composing the left flank of the anticline, below 2.5 km depth, are better imaged than in the reference images. There are also resolution improvements correlated with subtle stratigraphic features as, for example, the better imaging of the thin layers sequence around 2 km depth and position 4 km. These parts of the images are shown as zooms in the left column of Figure 5. Some structural features are also enhanced; for example, the strata truncations against the fault plane, around 1 km depth and position 6 km, are more evident in the weighted-PC RTM images than in the reference image, as shown in the zooms in the middle column of Figure 5. As a final example of resolution increase, observe that around the target region (2.5 km depth and position 6.5 km), the reservoir position at the top of an anticline and below a truncation sub-horizontal surface is better visible in the weighted-PC RTM images than in the reference image. This can be seen in

(a)

(b)
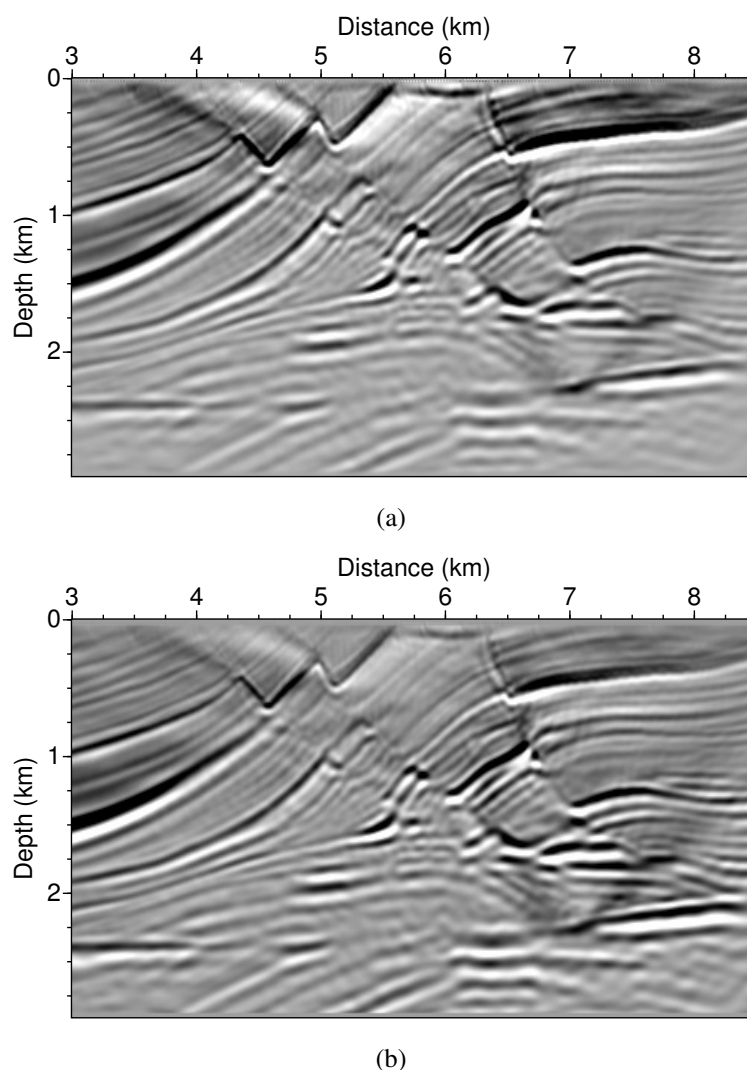
Figure 2: Classic cross-correlation RTM image (a) without and (b) with illumination compensation (conditions $I(\mathbf{x})$ and $I_{CC}(\mathbf{x})$ in equations 6 and 12, respectively).

more detail in the zooms in the right column of Figure 5.

The differences between the two weighted-PC images (Figure 4) are rather subtle. On the one hand, the envelope-weighted PC imaging condition (Figure 4b) appears to better delineate the fault and the stratigraphic geometry around the fault corners in the depth interval 0–1 km and position 5–7 km than its amplitude-weighted counterpart. A possible explanation is that the envelope weight imposes better stability on the PC image condition, because the envelopes present smoother variations than the amplitudes. On the other hand, the amplitude-weighted PC imaging condition (Figure 4a) brings out the finely layered dipping structures below the salt intrusion in the lower left corner of the image (superimposed on a horizontal artifact that is visible in all images).

Sensitivity parameter

The actual value of parameter ν is not very critical to the migrated result. We have noticed that increasing the value of ν promotes a slightly enhanced sharpness in the images resulting from equations 10 and 11. For comparison, we show in Figure 6 the amplitude-weighted PC RTM image obtained with $\nu = 1$ in
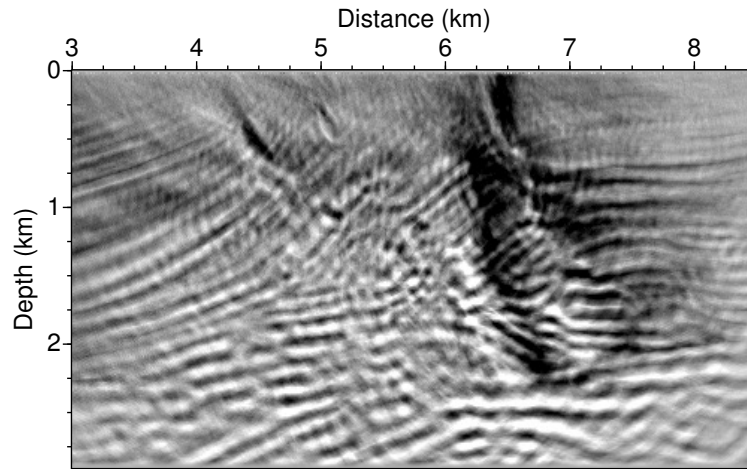
Figure 3: Phase cross-correlation RTM image (condition $I_{PC}(\mathbf{x})$ in equation 9) with $\nu = 100$.

equation 11 (compare with Figure 4a). Because the resolution is slightly better in Figure 4a, we chose $\nu = 100$ in our other numerical tests.

APPLICATION TO FIELD DATA SET

As a next step, we tested the proposed PC-based imaging conditions on a field dataset from a seismic line of a 2D land survey in the Solimãtes Basin (Amazon, Brazil) realized in 1984 as part of an exploratory program. Survey parameters were: 50 m source and receiver sampling, 241 sources, 96 channels in split-spread configuration, 3 s recording time, 4 ms sampling interval, 8–90 Hz field bandpass. The seismic data have a low-fold stack (maximum equal to 48). In the surveyed area, there exist two major problems for seismic processing. The first one is caused by a low-velocity zone, which makes it difficult to perform an adequate static correction. The second problem is caused by a relatively shallow basalt sill, which makes it difficult to obtain a good seismic imaging beneath it. As a consequence of both problems, a low signal-to-noise ratio is attained for the seismic events below the basalt sill. The amplitude equalization achieved by RTM with PC-based imaging conditions makes it a natural candidate in the attempt to enhance the seismic events in the deep portions of the image, below the basalt sill.

Before applying RTM, the seismic data were processed according to the following flow: static correction, geometrical spreading correction, amplitude correction to equalize the lateral spatial variation of the traces, spiking deconvolution, spectral balancing, residual static correction (trying to better correct relatively high frequency discontinuities), mute (on surface head waves), Radon transform (to interpolate missing traces), and band-pass filtering (10–60 Hz).

The RTM depth velocity model was built from a time migration velocity model through time-to-depth conversion using vertical rays. The model is represented on a uniform mesh with 6.25 m sampling interval. The source pulse is a Ricker wavelet with peak frequency 20 Hz, which reasonably approximates the true wavelet observed in the data.

Figures 7a, 7b, and 7c show the CC reference image (condition $I_{CC}(\mathbf{x})$ in equation 12), the amplitude-weighted PC image (condition $I_{PC}^p(\mathbf{x})$ in equation 10) and the envelope-weighted PC image (condition $I_{PC}^A(\mathbf{x})$ in equation 11), respectively. As before, the PC images were obtained with $\nu = 100$. Note that in this field-data example, the amplitude and envelope-weighted PC images are very similar, even more so than in the synthetic-data example. All existing differences are extremely subtle and have no significance regarding the quality of the images. For this reason, we restrict the following discussion to a comparison between the CC and the amplitude-weighted PC images.

To better visualize the differences between these two images, we present them in Figure 8 using a different visualization method, which uses an amplitude-volume processing technique (Bulhões, 1999; Bulhões and Amorim, 2005; Vernengo and Trinchero, 2015). Both the CC and PC images show strong-

(a)

(b)
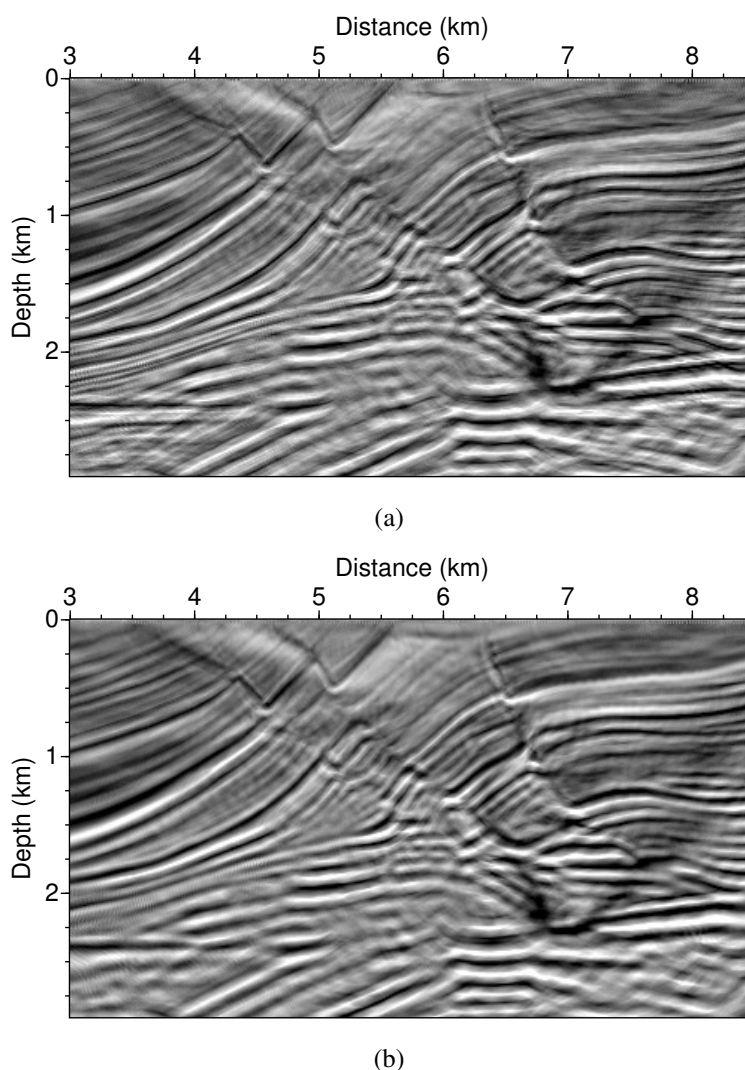
Figure 4: (a) Amplitude-weighted and (b) envelope-weighted phase cross-correlation RTM images (conditions $I_{PC}^{p}(\mathbf{x})$ and $I_{PC}^{A}(\mathbf{x})$ in equations 10 and 11, respectively) with $\nu = 100$.

amplitude reflection events at about 1 km depth, representing a shallow basalt sill. Below the sill, there are a number of differences between the two images. The most visible difference occurs below 2.5 km depth, where the PC image (Figure 8b) shows significantly enhanced amplitudes over the CC image (Figure 8a). In this deeper portion of the sections, both stratigraphic and structural features are hardly recognizable in the CC image, but are much better interpretable in the PC image. A prominent example is constituted by the subvertical faults at about 3 km depth and between horizontal positions 3 and 7 km. It is possible to interpret this portion of the section as composing a kind of "pull-up" geometry, limited by reverse faults (also compare this portion in the images of Figure 7). It is to be stressed that the existence of reverse faulting is in accordance with the known geology of the area (Ribeiro and Lima, 2007; Barata and Caputo, 2007).

Even above 2.5 km depth, where the CC and PC images have similar quality, they show different aspects of the same structures. For example, in the heavily faulted region between positions 7 and 10 km, certainly an interpreter would be more confident to locate the fault planes and infer the relative offsets with the additional information of the PC image at hand than using just the CC image, because several events are more easy to follow in the PC image.
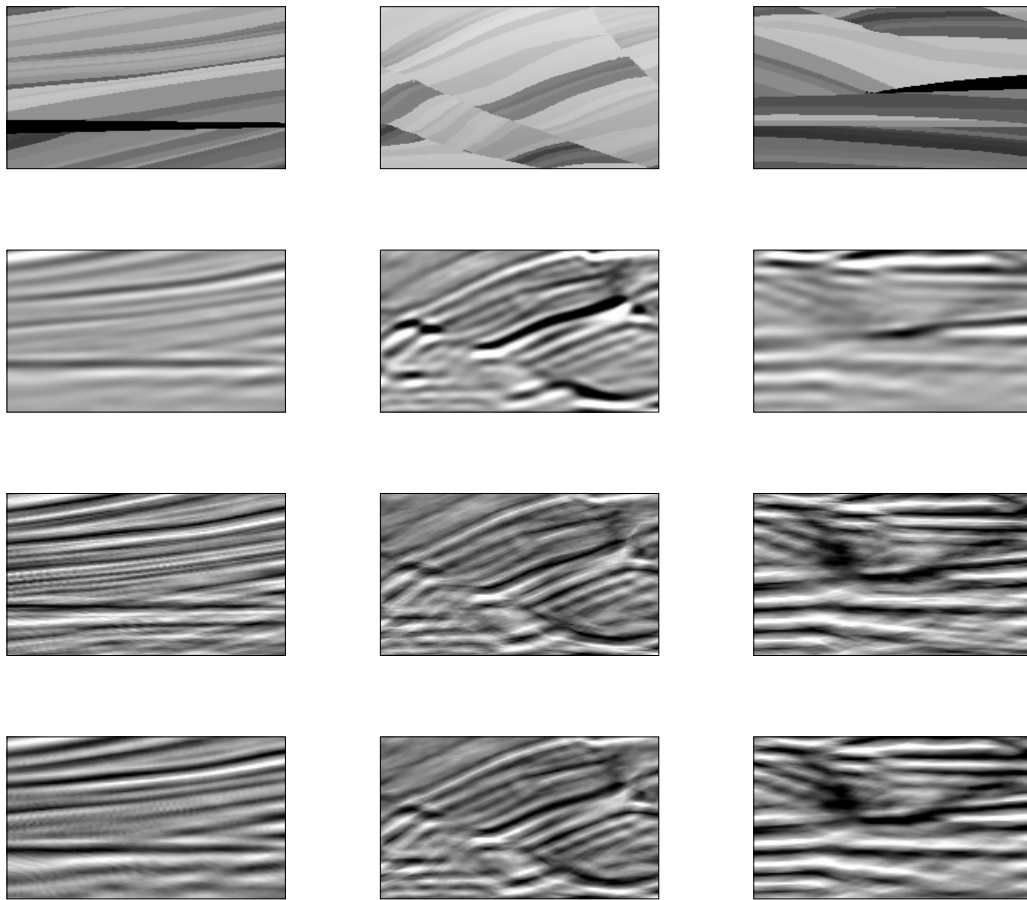
Figure 5: Panel showing in the rows, from top to bottom, four selected zooms from the true Marmousi model in Figure 1a, the reference CC image (with illumination compensation) in Figure 2b, the amplitude-weighted PC image in Figure 4a, and the envelope-weighted PC image in Figure 4b. Left, middle, and right columns show zooms centered around points (3.60 km, 2.15 km), (6.20 km, 1.15 km), and (7.05 km, 2.25 km), respectively.

DISCUSSION

The phase cross-correlation imaging conditions presented in this work rely on the availability of the analytical signals of the source and receiver wavefields. Although the numerical propagation of the analytical signals is slightly more expensive than of their real counterparts, their knowledge is desirable for other purposes as well. For example, they can be used to decompose the wavefields into up and downgoing constituents, which allows for the correlation of selected components to reduce backscattering (Shen and Albertin, 2015). An efficient procedure for the analytical-wavefield propagation has been proposed by Pestana and Revelo (2017). In this work, we have refrained from applying wavefield separation because we wanted to compare the PC imaging conditions to classical (real) cross-correlation, which does not allow for this kind of decomposition.

Our main result is that the PC-based imaging conditions can help to improve the resolution and visibility of weak reflections, particularly in deeper regions of the model. This is in agreement with the findings of Schimmel (1999), who observes that PC shows higher sensitivity to coherence than classical CC regardless
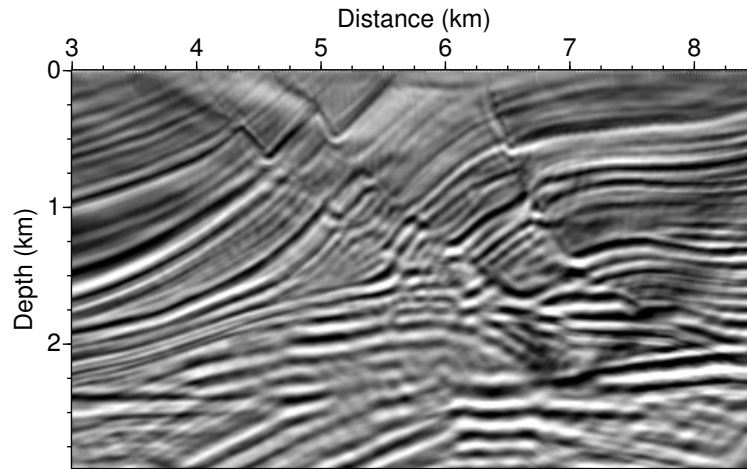
Figure 6: Amplitude-weighted phase cross-correlation RTM image (condition $I^p_{PC}(\mathbf{x})$ in equation 10) with $\nu = 1$.

of the event amplitude, and of Barnes (2007), who notes that instantaneous phase as a seismic attribute produces finer layering details and improved reflection continuity. In fact, Barnes (2007) points out that instantaneous phase carries no amplitude information at all and, in this sense, acts like a kind of perfect automatic gain control (AGC), completely equalizing amplitudes.

CONCLUSIONS

Classical and phase cross-correlations are independent approaches that provide complementary focusing criteria for RTM. Both full-wavefield and phase cross-correlations show maxima whenever there is waveform similarity, that is, whenever the migrated wavefields coincide in space and time at a scattering point in the subsurface. However, the phase coherence is sensitive just to waveform changes (and insensitive to waveform amplitude). Because of these properties, its inclusion into RTM can provide interesting additional information in the migrated images. Our numerical experiments on synthetic and field data indicate that the use of PC-based imaging conditions can lead to a refinement of the detected reflectors, allowing to increase resolution and reflector visibility, particularly in the deeper portions of the seismic images. In addition, the resolution gain can help to also enhance stratigraphic and structural features. In this way, the new imaging conditions can be instrumental to seismic interpretation.

The purely PC-based imaging condition is sensitive only to instantaneous phase changes and does not depend on the reflection amplitudes. This may lead to an enhancement of migration artifacts. Amplitude-weighted variations of this imaging condition preserve the desired properties of improving resolution while avoiding the enhancement of migration artifacts.

The PC-based imaging conditions can be computed simultaneously with conventional imaging conditions, once the analytical signals of the source and receiver wavefields have been propagated. Although this mildly increases the cost of RTM, the additional cost is justified by the additional information obtained by the computation of several images with different imaging conditions in a single run. Moreover, the analytical wavefield can be used to decompose the involved wavefields into their up and downgoing components, allowing for the simultaneous calculation of further additional imaging conditions, e.g., to reduce backscattering noise.
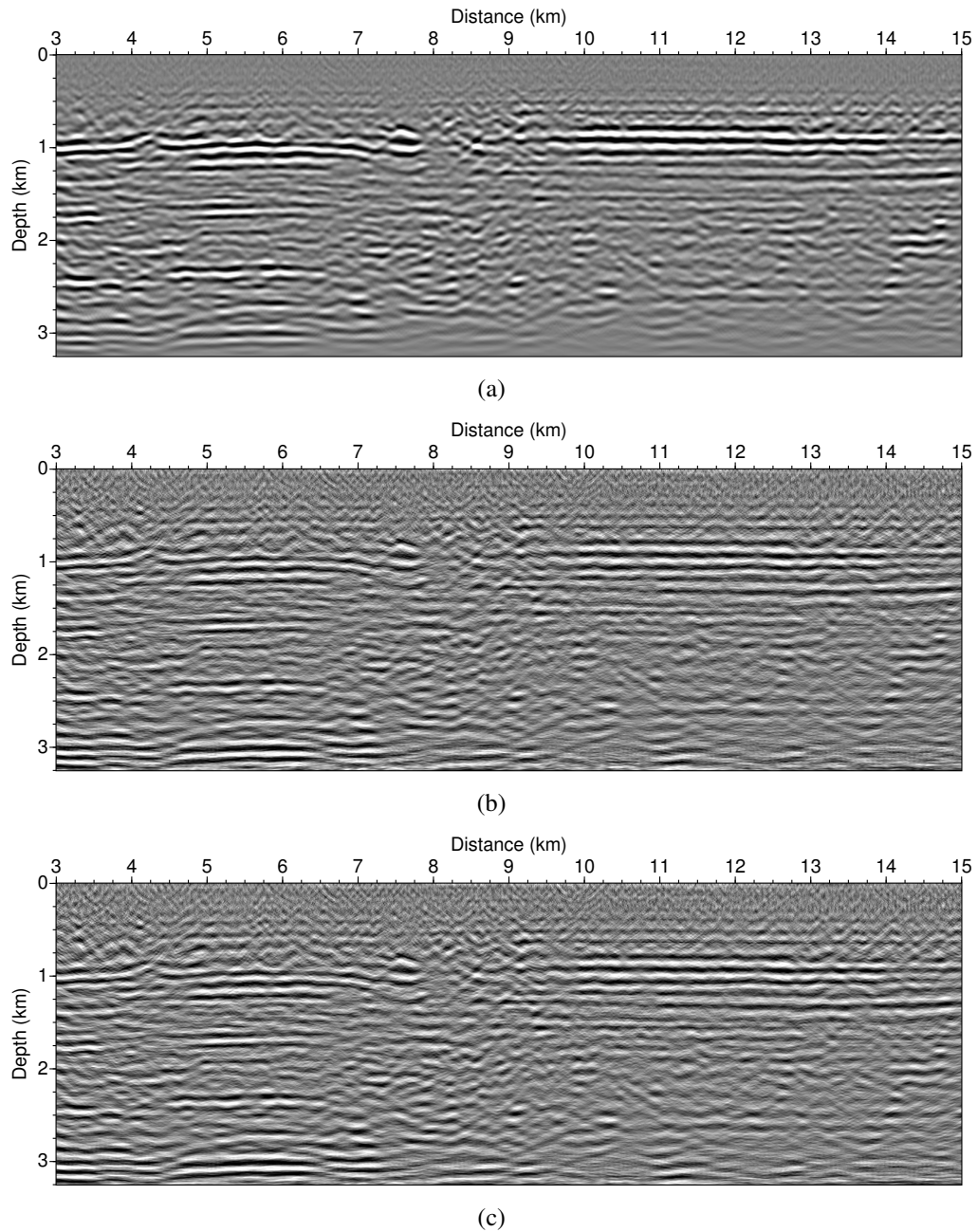
Figure 7: Field data: (a) Classic cross-correlation RTM image compensated for illumination (condition $I_{CC}(\mathbf{x})$ in equation 12). (b) Amplitude-weighted phase cross-correlation RTM image (condition $I_{PC}^{p}(\mathbf{x})$ in equation 10) with $\nu = 100$. (c) Envelope-weighted phase cross-correlation RTM image (condition $I_{PC}^{A}(\mathbf{x})$ in equation 11) with $\nu = 100$.

Distance (km)

(a)

Distance (km)

(b)
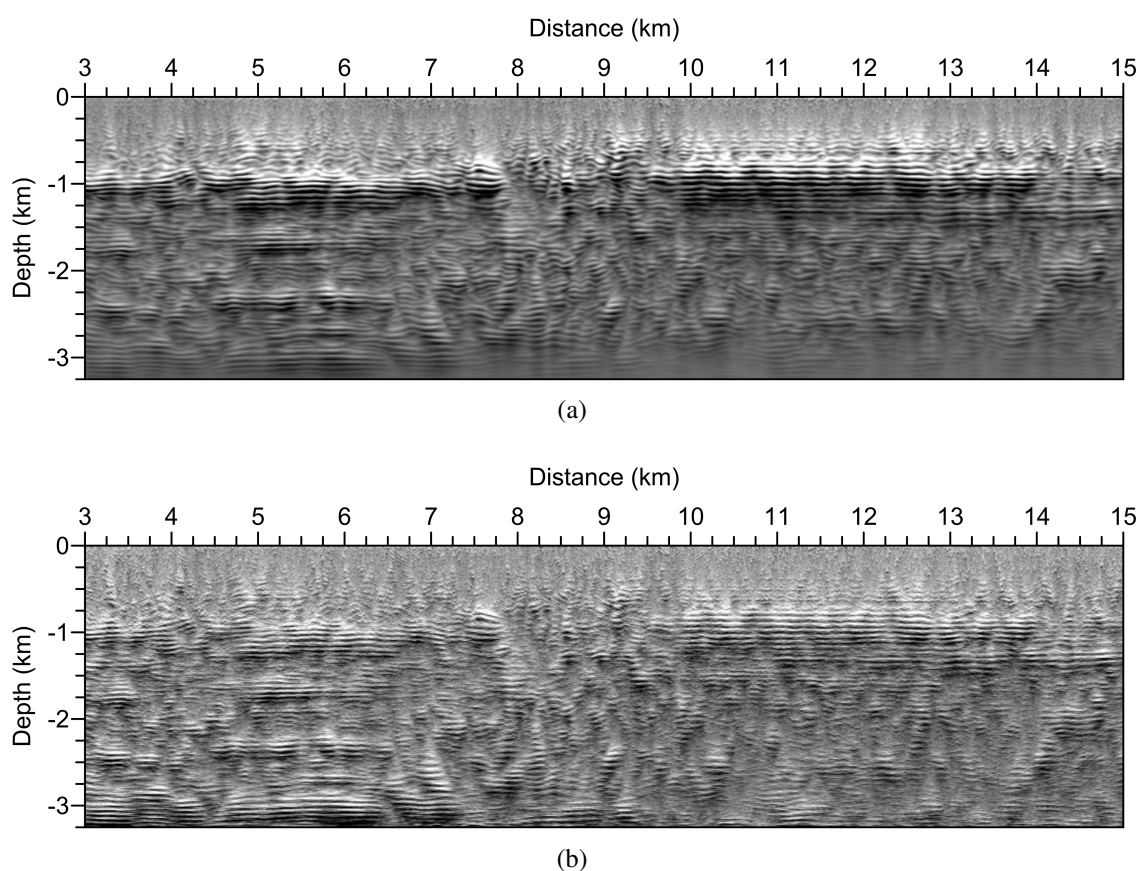
Figure 8: Field data: RTM images of Figure 7a and b in amplitude-volume-processing display: (a) CC imaging condition with illumination compensation; (b) amplitude-weighted PC imaging condition.

ACKNOWLEDGMENTS

REFERENCES

Barata, C. F. and Caputo, M. V. (2007). Geologia do petróleo da Bacia do Solimões. O "estado da arte". In 4º *PDPETRO, Proceedings*, pages 1.1.0147–1–1.1.0147–10. ABPG.

Barnes, A. E. (2007). A tutorial on complex seismic trace analysis. *Geophysics*, 72(6):no. 6, W33–W43.

Bonatto, L., Schimmel, M., Gallart, J., and Morales, J. (2015). The upper-mantle transition zone beneath the Ibero-Maghrebian region as seen by teleseismic PDS phases. *Tectonophysics*, 663:212–224.

Bracewell, R. N. (1965). *The Fourier transform and its applications*. Mcgraw-Hill.

Bulhões, E. M. (1999). Técnica "Volume de Amplitudes" para mapeamento de feições estruturais. In *6th International Congress of the Brazilian Geophysical Society*, page No. 296. SBGf.

Bulhões, E. M. and Amorim, W. N. (2005). Princípio da sismocamada elementar e sua aplicação à técnica de volume de amplitudes (TecVA). In *9th International Congress of the Brazilian Geophysical Society & EXPOGEF*, pages 1382–1387. SBGf.

Chattopadhyay, S. and McMechan, G. A. (2008). Imaging conditions for prestack reverse-time migration. *Geophysics*, 73(3):no. 3, S81–S89.

Claerbout, J. F. (1971). Toward a unified theory of reflector mapping. *Geophysics*, 36:467–481.

Costa, J. C., Silva Neto, F. A., Alcantara, M. R. M., Schleicher, J., and Novais, A. (2009). Obliquity-correction imaging condition for reverse time migration. *Geophysics*, 74(3):no. 3, S57–S66.

D'Hour, V., Schimmel, M., do Nascimento, A. F., Ferreira, J. M., and Lima Neto, H. C. (2015). Detection of subtle hydromechanical medium changes caused by a small-magnitude earthquake swarm in NE Brazil. *Pure and Applied Geophysics*, 173(4):1097–1113.

Du, Q., Guo, C., Zhao, Q., Gong, X., Wang, C., and Li, X.-Y. (2017). Vector-based elastic reverse time migration based on scalar imaging condition. *Geophysics*, 82(2):S111–S127.

Etgen, J., Gray, S. H., and Zhang, Y. (2009). An overview of depth imaging in exploration geophysics. *Geophysics*, 74(6):no. 6, WCA5–WCA17.

Gaudot, I., Beucler, E., Mocquet, A., Schimmel, M., and Le Feuvre, M. (2015). Statistical redundancy of instantaneous phases: Theory and application to the seismic ambient wavefield. *Geophysical Journal International*, 204(2):1159–1163.

Guitton, A., Valenciano, A., Bevc, D., and Claerbout, J. F. (2007). Smoothing image condition for shot-profile migration. *Geophysics*, 72(3):no. 3, S149–S154.

Haned, A., Stutzmann, E., Schimmel, M., Kiselev, S., Davaille, A., and Yelles-Chaouche, A. (2015). Global tomography using seismic hum. *Geophysical Journal International*, 204(2):1222–1236.

Holberg, O. (1987). Computational aspects of the choice of operator and sampling interval for numerical differentiation in large-scale simulation of wave phenomena. *Geophysical Prospecting*, 35(6):629–655.

Moradpouri, F., Moradzadeh, A., Pestana, R., Ghaedrahmati, R., and Monfared, M. S. (2017). An improvement in wavefield extrapolation and imaging condition to suppress reverse time migration artifacts. *Geophysics*, 82(6):S403–S409.

Pestana, R. P. and Revelo, D. (2017). An improved method to calculate the analytical wavefield for causal imaging condition. In *SEG Technical Program Expanded Abstracts 2017*, pages 4640–4644. SEG.

Ribeiro, R. B. and Lima, T. C. S. (2007). Evidência da tectônica do Juruá em linhas 2D reprocessadas da Bacia do Solimões. In 4º *PDPETRO, Proceedings*, pages 1.2.0206–1–1.2.0206–6. ABPG.

Sava, P. (2007). Stereographic imaging condition for wave-equation migration. *Geophysics*, 72(6):no. 6, A87–A91.

Schimmel, M. (1999). Phase cross-correlations: Design, comparisons, and applications. *Bulletin of the Seismological Society of America*, 89(5):1366–1378.

Schimmel, M. and Paulssen, H. (1997). Noise reduction and detection of weak, coherent signals through phase-weighted stacks. *Geophysical Journal International*, 130:497–505.

Schimmel, M., Stutzmann, E., and Gallart, J. (2010). Using instantaneous phase coherence for signal extraction from ambient noise data at a local to a global scale. *Geophysical Journal International*, 184(1):494–506.

Schleicher, J., Costa, J. C., and Novais, A. (2008). A comparison of imaging conditions for wave-equation shot-profile migration. *Geophysics*, 73(6):no. 6, S219–S227.

Shen, P. and Albertin, U. (2015). Up-down separation using Hilbert transformed source for causal imaging condition. In *SEG Technical Program Expanded Abstracts 2015*, pages 4175–4179. Society of Exploration Geophysicists.

Vernengo, L. and Trinchero, E. (2015). Application of amplitude volume technique attributes, their variations, and impact. *The Leading Edge*, 34(10):1246–1253.

Wang, W., McMechan, G. A., Tang, C., and Xie, F. (2016). Up/down and P/S decompositions of elastic wavefields using complex seismic traces with applications to calculating Poynting vectors and angle-domain common-image gathers from reverse time migrations. *Geophysics*, 81(4):S181–S194.

Yan, J. and Dickens, T. A. (2016). Reverse time migration angle gathers using Poynting vectors. *Geophysics*, 81(6):S511–S522.

Yoon, K. and Marfurt, K. (2006). Reverse-time migration using the Poynting vector. *Exploration Geophysics*, 37(1):102.

Zhang, Y. and Sun, J. (2009). Practical issues in reverse time migration: True amplitude gathers, noise removal and harmonic source encoding. *First Break*, 26(1):January, 29–55.

Zhang, Y., Sun, J., and Gray, S. (2007). Reverse-time migration: Amplitude and implementation issues. In *SEG Technical Program Expanded Abstracts 2007*, pages 2145–2149. SEG.